Mass and charge transport kinetics in an organic mixed ionic-electronic

conductor

3

1

2

4 Ruiheng Wu, ¹ Bryan D. Paulsen, ² Qing Ma, ³ Jonathan Rivnay^{2,4*}

5

- ¹Department of Chemistry, Northwestern University, Evanston, IL 60208, USA
- ²Department of Biomedical Engineering, Northwestern University, Evanston, IL 60208, USA
- ³DND-CAT, Synchrotron Research Center, Northwestern University, Evanston, IL, 60208, USA
- 9 ⁴Simpson Querrey Institute, Northwestern University, Chicago, Illinois 60611, USA
- 10 E-mail: jrivnay@northwestern.edu

11

12

Abstract

Understanding the mass uptake, morphological changes, and charge transport in organic mixed 13 14 ionic-electronic conductors (OMIECs) during device operation is crucial for applications in energy, actuators, and bioelectronics. In this work, we quantify the chemical composition and rheological 15 16 properties of a model OMIEC material, acid treated poly(3,4-ethylenedioxythiophene) polystyrene sulfonate (PEDOT:PSS), during electrochemical cycling using electrochemical quartz crystal 17 microbalance (EQCM) and elemental analysis techniques. We find an asymmetry in the de- and 18 re-doping mass transport kinetics and attribute this process to sub-second ion migration and slower 19 20 ion reorganization. Furthermore, the kinetic constants from the EQCM measurements are compared to those from organic electrochemical transistors and from changes in structural packing 21 22 by normalizing the corresponding RC time constants across experiments/techniques. This multimodal investigation allows us to deduce a sequence of mass, charge, and structure kinetics in 23 OMIEC materials during the de- and re-doping processes. The kinetics of processes in acid treated 24 25 PEDOT:PSS in response to step voltages can be clustered into three main sub-processes, namely: fast polarization, charge carrier population kinetics and macroscale transport, and slow relaxation. 26 These findings provide a basis for future OMIEC design by determining the factors that affect 27 response time and short-term stability of OMIEC devices. 28

Introduction

1

Organic mixed ionic-electronic conductors (OMIECs) are conjugated materials that transport 2 electronic charges, and readily uptake and transport ionic charges. The ionic conduction and ionic-3 electronic coupling makes OMIECs attractive for energy storage,^{2, 3} light emitting devices,⁴⁻⁶ 4 actuators⁷ and bioelectronics.^{8, 9} One important implementation for OMIECs is in organic 5 electrochemical transistors (OECT). where the organic semiconductor film is directly in contact 6 with and gated by an electrolyte, which enables both fundamental studies of transport as well as 7 bioelectronic application. 10-12 OMIECs show volumetric capacitance allowing ions from the 8 electrolyte to compensate charges on the polymer backbone, and thus are ideal OECT channel 9 materials for high gain and actuation. 10 and highly studied OMIEC acid treated poly(3,4-11 prototypical material is ethylenedioxythiophene) polystyrene sulfonate (PEDOT:PSS).¹³ To achieve high performance, 12 pristine PEDOT:PSS usually requires extra additives or post-treatment to improve its conductivity 13 and stability. 14-17 In particular, concentrated strong acids (H₂SO₄, H₃PO₄, etc) selectively dissolve 14 excess PSS and recrystallize the PSS templated PEDOT. 13, 18, 19 Due to the high crystallinity for a 15 conjugated polymer and 3D crystalline network, 19 the acid treated PEDOT:PSS has been reported 16 for the highest electrical conductivity in OMIECs (4380 S cm⁻¹) and µC* (the product of mobility 17 and volumetric capacitance), ¹³ a figure of merit of OECT transconductance. ²⁰ The material is 18 readily processable into different geometries for various applications, such as thin films, 13, 21 19 fibers²² and free standing electrodes.^{23, 24} Acid treated PEDOT:PSS is a promising model system 20 for OMIEC studies, not only because of its high OECT performance, but also for the 21 compositional/structural simplicity. There is no requirement for extra additives, such as ethylene 22 glycol, dimethyl sulfoxide, ionic liquids, surfactants and crosslinker. The high crystallinity and 23 phase purity of acid treated PEDOT:PSS simplify the structural and kinetic models compared to 24 other semi-crystalline OMIECs. 25 Previous studies have focused on the characterization of electronic/ionic transport and structural 26 change that are important to OMIEC devices compared to traditional conjugated polymer-based 27 devices.²⁵ In aqueous electrolytes, ions together with water readily interact with the materials, 28 which lead to ionic-electronic coupling. The process is accompanied by significant structural 29 changes, ranging from microscale crystalline stacking, 26 and mesoscale 27 to macroscopic 30

swelling.^{28, 29} For acid treated PEDOT:PSS, the electronic properties have been characterized in

thin films and fibers by measuring stain dependent electronic conductivity and $\mu C^{*,22,30}$ showing

3 both improved electronic mobility and volumetric capacitance after acid treatment.²² Electron

microscopy and atomic force microscopy have revealed well-crystallized nanofibers, ^{18, 21, 23, 24} and

5 ex situ XRD provides the molecular spacings and orientation of these crystallites.^{19, 22} In addition,

6 both XPS and optical absorption spectroscopy confirm the removal of PSS with acid treatment. 13,

^{18, 22} However, these measurements are carried out in steady state or ex situ, which considerably

8 differs from the transient/dynamic state in most of OMIEC applications.³¹

4

7

9

10

11

12

13

14

15

16

17

18

19

20

21

22

23

24

25

26

27

28

29

30

To reveal the structure-property relationship in real operation conditions, recent studies have begun to tackle the transient kinetics of OMIECs. Paulsen et al. have probed the microstructural kinetics of acid treated PEDOT:PSS by operando GIWAXS, and related the structural kinetics with charge population kinetics by spectroelectrochemistry. 26 Similar time-resolved optical measurements were reported by Rebetez et al. for PEDOT:PSS with EG added, arguing that ion diffusion might not be the limiting parameter for the redox process in OMIEC films.³² Direct characterization of electron and mass transport kinetics is more important to OMIECs. Physical models of OECTs under transient voltage steps have been developed, and the electronic transport transients can be readily converted via LaPlace transform from frequency dependent data measured from devices.³³-³⁵ Compared to electronic transport, mass transport kinetics are more difficult to access. In-plane ionic transport has been probed using optical spectroscopic analysis of electrochromic moving fronts in end-biased OMIECs.^{27, 36, 37} This method only measures the transport of net ionic/electroactive species and cannot deconvolute different ions and water. Due to the geometry of the setup, this method is difficult to translate for most device geometries. Electrochemical quartz crystal microbalance with dissipation monitoring (EQCM-D) can be used to track mass, thickness and mechanical property variation of OMIEC thin films.^{29, 38-42} This technique has been successfully applied on P3HT to reveal the slow mass transfer kinetics during electrochemical doping. 43, 44 Despite the lack of effective deconvolution between water and ions, this method has a time resolution less than 1s and is adequate for monitoring the mass transport kinetics in commonly used OMIECs.

Herein, we focus on the mass and electronic transport transient of the model OMIEC material, acid treated PEDOT:PSS. We employ time-resolved EQCM-D to reveal the mass transfer and its

- related mechanical kinetics during operation. The mass transport at different depths is probed by analyzing different overtones. These results were combined with charging dynamics and ex situ
- 3 elemental analysis methods (XPS, XRF) to reveal different ions participating the electrochemical
- 4 cycling process and to deconvolute the mass changes due to ions and water. Additionally, transient
- 5 OECT experiments were performed to monitor channel conductivity and hole mobility transients.
- 6 By normalizing these transient data with experimental RC time constants, 45 we related the kinetics
- 7 of ion transport, water transport, hole transport, and mechanical properties along with our previous
- 8 data on kinetics of polaron/bipolaron transformation and microstructural molecular packing.⁴⁶
- 9 Finally, we find that the mass and rheological transients are the fastest steps following by a slow
- 10 charge transfer. On longer time scales, the charge within the film undergoes reorganization and
- eventually converges to an equilibrium state after a slow relaxation.

13

14

Experimental section

Materials and sample preparation:

- 15 PEDOT:PSS (Clevios PH-1000), purchased from Heraeus Holding GmbH, was filtered through
- 16 0.45 µm PES filters to remove large particles. For EQCM-D samples, the filtrate was spin-coated
- on QCM chips (Quartz PRO, 5.000 MHz, 14mm Ti/Au) for 1000 rpm for 4 minutes, following
- by 3000 rpm for 10 s to remove extra solution on the edge. For the thick samples that simulate
- 19 the bulk film, the chip was heated at $70 \, ^{\circ}$ C for 1 minute and the spin-coating process was
- 20 repeated for 6 times. The cast films were dried in ambient at 120 °C for 10 minutes to fully
- 21 remove water and then immersed into concentrated H₂SO₄ (Sigma-Aldrich, 95.0% 98.0%) at
- room temperature for 10 minutes (for 1-layer thin samples) and 60 minutes (for 6-layer thick
- samples), respectively. The films were rinsed with DI water for 3 times after acid treatment and
- 24 then dried in ambient at 120 °C for 10 minutes. For XPS and XRF samples, the filtrate was drop-
- casted on degenerately p-doped Si wafer (0.001-0.005 ohm cm⁻¹) (University Wafer) at 70 °C
- that had been successively sonicated in acetone and isopropyl alcohol, and exposed with UV-
- ozone prior to drop-casting. For pseudo-OECT samples, the films were drop-casted on glass
- substrate following the same method described above. Due to the thickness of the drop-cast film,
- all drop-casted films were dried at 120 °C for 20 minutes and the acid treatment time was

- prolonged to 3 hours. After rinsing in DI water, the samples were first heated at 60 °C for 30
- 2 minutes and then 120 °C for 30 minutes in ambient to form homogenous metallic purple films.
- 3 **EQCM-D measurement:** EQCM-D was performed using a potentiostat (Ivium) connected with
- 4 a QSense electrochemistry module. Three-electrode setup comprised a Ag/AgCl reference
- 5 electrode, Pt counter electrode, and the EQCM chips with Au coated (0.785 cm²) as the working
- 6 electrode. All data analysis and model simulation were performed with Matlab software.
- 7 X-ray photoelectron spectroscopy measurement: The XPS spectra were taken using Thermo
- 8 Scientific ESCALAB 250Xi equipped with a monochromatic KR Al X-ray source (spot size of
- 9 900 μm) at the Northwestern University Atomic and Nanoscale Characterization Experimental
- 10 center (NUANCE). For depth profile, each ionic beam etching time was set at 120s (~600nm).
- 11 Before data collection, a flood gun was used for charge compensation. The curve fitting was
- 12 performed with the Avantage (Thermo Scientific) software. All the ex situ samples were rinsed
- in DI water for three times to avoid the remained external electrolyte on sample surface.
- 14 X-ray fluorescence measurement: The XRF measurements were carried out at the 5-BM-D
- beamline located at Sector 5 of the Advanced Photon Source (Argonne, Illinois). A Si (111)
- monochromator is used for X-ray energy selections. The incidence X-ray beam intensity is
- monitored using the spectroscopy-grade ionization chamber (FMB-Oxford). The X-ray beam
- size on the sample is 1.0×6.0 (V×H) mm. The X-ray beams with the energies of 15,000 eV and
- 19 15,250 eV are used, respectively, to excite the samples, which are 200 eV below and 50 eV
- above the Rb K absorption edge (15,200 eV). This allows decouple the overlapping Br K_{β} and
- 21 Rb K_α peaks. The X-ray fluorescence spectra were recorded using a 4-element Si-drift solid state
- detector (Hitachi, USA) equipped with a 4-channel xMAP digital X-ray processor. All data
- 23 analysis was performed with Matlab software. All the ex situ samples were rinsed in DI water for
- three times to avoid the remained external electrolyte on sample surface. Calibration samples
- 25 were made from thiourea and RbBr mixtures spin coated on Si substrates (1200rpm), with S to
- 26 ion ratio of 1:1, 1:4, 1:16, 1:80 and 1:160.
- 27 **OECT transfer curve measurement:** Transistors were tested in ambient conditions using a
- 28 potentiostat (Ivium) and recorded using IviumSoft. OECTs underwent four transfer curves in the
- 29 diode-connected configuration with a scan rate of 250 mV/s to ensure reproducible current—
- 30 voltage behavior.

- **Pseudo-OECT samples:** The patterned pseudo OECT samples were placed in the same cone
- 2 cell as in the previous study, ²⁶ and 2mL 0.1 M NaCl was sealed in the chamber over the sample.
- 3 The setup was connected in the three-terminal configuration, and the gate, source and drain
- 4 current curves were recorded using a potentiostat (Ivium).

Results and discussion

To understand the mass transfer dynamics of acid treated PEDOT:PSS, the resonant frequencies together with the dissipation of material-coated piezoelectric crystal sensors (quartz chip with Au deposited) were monitored in situ during stepped electrochemical potentials. Sensors were coated with six spin-coated PEDOT:PSS layers prior to acid treatment to better mimic the drop-cast materials used in previous reports²⁶ while avoiding delamination. The acid treatment has been reported to have no effect on the performance of the QCM sensors.⁴⁷ Single layer spin coated PEDOT:PSS films were also used in EQCM-D studies for quantitative mass transport analysis. Quantitatively, the resonant frequency shift recorded by the EQCM-D follows an inverse trend to the mass change, i.e., an increase in resonant frequency indicates a decrease in film mass.⁴⁸

Because of the negative frequency shift in EQCM-D measurement, a larger frequency difference

 $(f_t - f_0)$ means a larger gain in mass, which is described by the Sauerbrey equation (**Equation 1**):

$$\Delta f_{Sauerbrey,n} = \frac{2nf_1^2}{Z_q} \Delta M \tag{1}$$

Where $\Delta f_{sauerbrey,n}$ is the Sauerbrey frequency shift for nth order overtone, and ΔM is the change in mass. The constant f_1 is the fundamental frequency of the QCM chip and Z_q is the acoustic impedance of the quartz crystal. The dissipation of the frequency signal is related to the mechanical properties of the film, and a sample in air with increased dissipation is generally considered to be softer. However, hydrated films in water show complex viscoelastic behavior. Depending on the geometry and mechanical/rheological properties of the films, the mass change might need to be quantified with appropriate viscoelastic models. In the case of single spin-coated layers, the results of both Sauerbrey and viscoelastic models were comparable (See the discussion in SI Part 2).

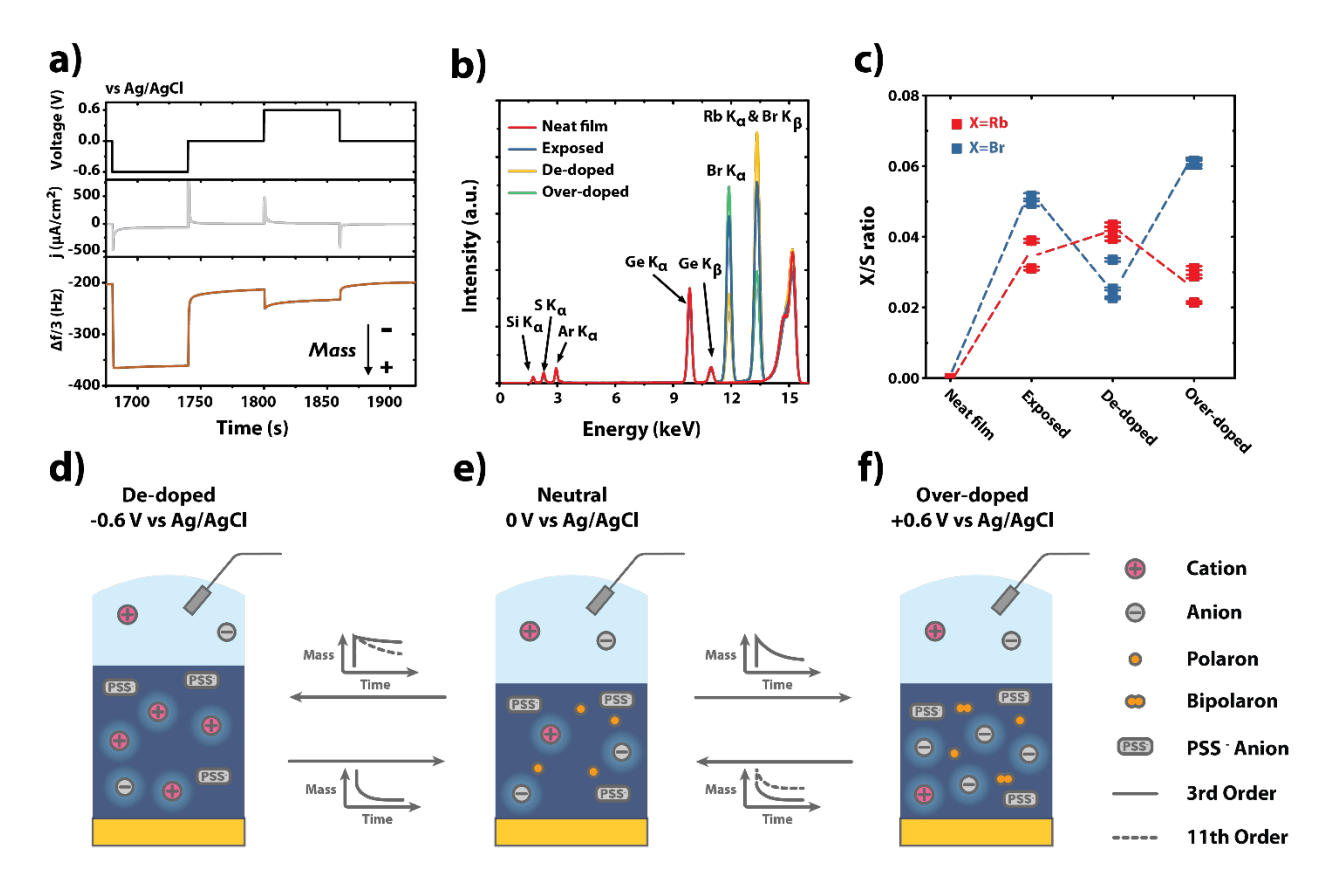


Figure 1. Mass and compositional changes during electrochemical cycling. a) Single electrochemical cycle in EQCM after reaching quasi-stable state, showing the stepped potential (black line), current density (grey line) and the frequency shift of 3rd order overtone (brown); b) the XRF spectra of pristine (red), naturally doped state (blue), de-doped state (yellow) and overdoped state (green); c) the ratio of doping ions and sulfur atoms for the above four states. Schematic diagram of acid treated PEDOT: PSS in d) de-doped state (-0.6V vs Ag/AgCl) e) naturally doped state (0V vs Ag/AgCl) and f) over-doped state (0.6V vs Ag/AgCl). The blue gradient around the ions within the OMIECs represents the water shell.

To maintain consistency with previous studies, three states of acid treated PEDOT:PSS were selected for electrochemical cycling, namely naturally doped state (0V vs Ag/AgCl, \sim -0.2V vs open circuit potential, OCP), de-doped state (-0.6V vs Ag/AgCl) and over-doped state (+0.6V vs Ag/AgCl). The four steps between these three states are known as de-doping (0 to -0.6 V vs Ag/AgCl), re-doping back to 0V (-0.6 to 0 V vs Ag/AgCl), over-doping (0 to + 0.6 V vs Ag/AgCl) and de-doping back to 0V (+0.6 to 0 V vs Ag/AgCl). The acid treated PEDOT:PSS films were first

- 1 exposed to aqueous electrolyte, where film mass increased due to ion exchange and water uptake.
- 2 After reaching mass transport equilibrium, in which the material swelled ~33% in mass (**Figure**
- 3 S1a, from viscoelastic model) compared to the dry state (thickness from profilometer listed in
- 4 Figure S1b), step voltages were applied to the material. During initial cycles, film mass further
- 5 increased and finally equilibrated after 4-5 cycles (using 3rd order frequency, shown in **Figure S2**).
- 6 The equilibrated negative frequency shift following these cycles indicates a stabilized mass
- 7 increase, likely due to a further ion exchange between the electrolyte and polymer film that leads
- 8 to the permanent ion accumulation. The equilibrated state was used as a baseline for comparison
- 9 during the further electrochemical cycling.
- 10 The degree of swelling of the film in electrochemical equilibrium relates to the applied potentials,
- which constitute the quasi-stable (equilibrium) endpoints in the transient measurement experiment,
- as shown in **Figure 1a**. While the degree of swelling in the de-doped and re-doped states depended
- on applied potential, the degree of swelling in the over-doped state was shown to be further
- sensitive to the film OCP (**Figure S3**). In the naturally doped state of the film (0V vs Ag/AgCl),
- 15 further swelling of ~6% compared to the exposed state was accompanied by an increase in
- dissipation, implying that the trapping of ions makes the film thicker and more viscoelastic. A
- significant decrease in EQCM frequency (increase in mass) was observed for both de-doped and
- over-doped states relative to the naturally doped state (**Figure S4**). When a bias voltage of -0.6 V
- 19 vs Ag/AgCl was applied, the holes in the material were extracted. The metal cations in aqueous
- 20 electrolyte replaced the positively charged holes in the material, triggering the expected mass
- 21 increase. This state is the most swelled and shows the largest dissipation of the three biasing
- 22 conditions, implying that the de-doped state is the softest state among the three. When a bias
- voltage of +0.6 V vs Ag/AgCl was applied, the material was further electrochemically oxidized
- 24 and reached the over-doped state. The mass increase in this state can be attributed to the charge
- balance of the anion (not enough PSS⁻) that is needed to compensate the newly generated holes in
- the material.
- 27 For single layer spin coated thin films (~40nm, **Figure S1a**) that can be quantitatively analyzed by
- EQCM, we are able to deconvolute the mass of water, cations, and anions by combining the current
- 29 signals and elemental analysis. The composition deconvolution in previous EQCM work was
- based on a number of assumptions made in OMIECs, such as the complete ion replacement of

holes at the maximum doping level and a fixed ion/water ratio, but without support on elemental 1 analysis.²⁹ For frequency shift in EOCM measurement, the results from the Sauerbrev equation 2 3 and viscoelastic model are shown in Figure S5, from which the Sauerbrey equation slightly underestimates the mass change during the cycling. The following discussion is based on the 4 viscoelastic model due to the viscoelastic nature of the OMIEC film. In the de-doped state, the 5 mass of single layer thin film increased by $\sim 0.8 \mu g/cm^{-2}$ compared to the naturally doped state; in 6 7 the over-doped state, the film mass increased by $\sim 0.15 \,\mu \text{g/cm}^{-2}$ compared to the naturally doped state. The transient current and EQCM frequency was also measured across electrochemical 8 9 potential steps, showing a current spike and the subsequent exponential decay as potential step applied on the material. From the analysis of the transient current, the mass change calculated from 10 the EQCM frequency shift (and its dissipation) cannot be accounted for by the mass of the cations 11 12 alone. Using the de-doping process for example, the expected mass increase calculated from the transient current assuming only cations participate in de-doping (0.4 µg/cm⁻²), is still smaller than 13 the total weight gain of the film (0.8 µg/cm⁻²) from EQCM frequency shift. In fact, over 80% of 14 the mass change happened within the first few hundred milliseconds, which corresponds to the 15 16 spike in the current signal. The maximum cation mass increase calculated from the current spike is 0.02 µg/cm⁻². This implies the transport of a large amount of water (larger than 4 water molecules 17 per cation reported in previous study)²⁹ along with the solvated cations into the film. 18 Therefore, additional elemental analysis methods, including ex situ X-ray fluorescence (XRF) and 19 X-ray photoelectron spectroscopy (XPS) were performed to assess the ion to thiophene ratio. The 20 XRF results are shown in Figure 1b,c, where RbBr solution instead of NaCl was used as the 21 22 electrolyte to match the hard X-ray source and achieve a better resolution. The similar mass transport behavior between metal halides was proven by XPS of films immersed in NaCl solution 23 (Figure S6). The EQCM measurements (Figure S5 and Figure S7) and OECT transfer curves 24 (Figure S8) of single layer PEDOT:PSS films in both RbBr and NaCl solution are also consistent 25 with each other. The XRF data gives quantitative insights into the elemental composition of the 26 27 films in different doping states. Ions per thiophene in each sample were calculated from XRF peak ratios (calibrated against known composition films). Related ion mass per area was calculated from 28 the XRF-determined concentration using the initial film thickness and an assumed density of 1.0 29 g·cm⁻³. In the naturally doped state, more anions (both PSS⁻ and Br⁻) than cations were present in 30

the film to balance the extra holes in the acid treated PEDOT:PSS (Figure 1e). In the entire

electrochemical cycle, both anions and cations were involved, consistent with previous QCM and 1 XRF studies of OMIECs and conjugated polymers. 44, 54-56 Based on our XRF analysis, when the 2 3 material was de-doped, cations (0.01 per thiophene, 0.01 µg/cm⁻²) entered the film, while a large number of anions (0.02 per thiophene, 0.02 µg/cm⁻²) left the film (**Figure 1d**). From this result, 4 the cations carried more solvated water, causing the film to exhibit significant overall swelling. 5 When the film was over-doped, more anions (0.03 per thiophene, 0.03 µg/cm⁻²) re-entered the film 6 and extra cations (0.01 per thiophene, 0.01 µg/cm⁻²) were expelled (**Figure 1f**). Despite the 7 8 possible underestimation in these ex situ measurement (the loss of non-electrostatic bonded ions 9 upon DI rinsing), quantitative calculations from XRF data also show that the mass change from dopant ions only occupies a small fraction of the total mass change, indicating significant water 10 11 transport during the electrochemical cycling. 12 The time-resolved measurements of EQCM frequency shift reveals the kinetics of the mass 13 transport in OMIECs, and the simultaneous current measurements capture the charge transients. 14 An applied potential step results in a current spike and the subsequent exponential decay, from which the RC time constant can be fitted. The mass and charge transport kinetics of OMIEC films 15 16 in de-doping and re-doping processes as expressed in QCM frequency shifts and normalized charge density changes in response to applied potential steps are plotted in Figure 2a&b. In 17 18 comparison, the frequency shift can be divided into two parts, a fast, sub-second step followed by 19 a slow step lasting several to tens of seconds. For both de-doping (the original state in Figure 2c-1) and re-doping processes (the original state in Figure 2d-4), the fast step has the largest 20 magnitude of mass change and occurs within less than half of the RC time constant (charge 21 22 accumulation) of the film (Figure 2c-2, Figure 2d-5). This process may arise from an 23 instantaneous non-equilibrium ion migration due to the suddenly changed electric field. Ions and water are attracted/repelled by the field induced by the polarizable buried Au electrode. Previous 24 25 studies claiming that the ion migration is the limiting factor on device response time are inconsistent with the following observations.⁵⁷ The hole extraction/injection happening after the 26

the mass change of this process can be the same or opposite to the fast process, depending on the

fast mass transport leads to the equilibrium state, following with a slow concurrent ion/water

reorganization (Figure 2c-3, Figure 2d-6). The slow process has a smaller magnitude compared

to the fast process and the resonance frequency always increases, implying the loss of mass. Thus,

27

28

29

30

from the structural relaxation, ionic migration and reorganization after injection of electronic charge.

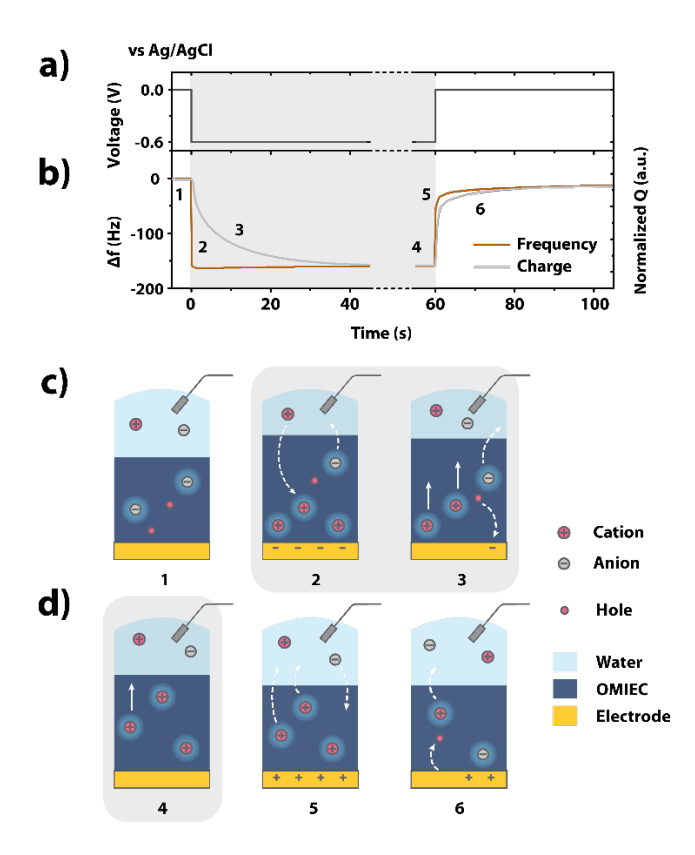


Figure 2 a) The potential profile for de-doping and re-doping process; b) Different step of charging curve (grey), 3rd overtone frequency shift (brown). Schematic pictures of the step order occurring during c) de-doping process and d) re-doping process. The blue gradient around the ions within the OMIECs represents the water shell. The dotted white arrows represent ion/charge migration across the interface, and the solid white arrows represent the ion/water reorganization that will be discussed later. The "+" and "-" are used to represent the unbalanced positive and negative electric field. The de-doping process is highlighted with gray background.

Compositional Depth Dependence

To get a deeper insight into the ionic transport within OMIEC films, thicker films (formed by successive spin coating and soft baking of 6 layers, ~220 nm in dry state, **Figure S1c-d**) were investigated. The voltage profile and the recorded current are plotted in **Figure 3a&b**. For thicker films, the use of Sauerbrey equation produces a large deviation among the results based on

different EQCM overtones (Figure S9c). While the viscoelastic model also did not give quantitative fits, qualitative analyses of the frequency shift from different overtones gave insight into the thickness dependent mass changes. In general, the higher order shear waves are more sensitive to the material close to the electrodes, while the lower order waves damp less in the film, thus reflecting the bulk properties of the film (Figure 3d).^{48, 58} With a vertical mass/density gradient, there is a difference between the effective mass detected by the higher order waves and that of the lower order waves (discussed in detail in SI Part 2, also Figure S9). The difference between the different order overtones becomes more pronounced in a thicker film (Table S2). For the single-layer thin film, no significant order-dependent differences were observed in the electrochemical cycles (Figure S4) because the attenuation of different overtones (from 3rd order to 11th order) is not pronounced in the thin film. For thicker films, the higher order overtones exhibit greater frequency shifts (implying greater mass changes deeper in the film) compared to the lower order overtones (Figure 3c and Figure S10), both for individual de-doping/re-doping processes and for the overall mass increase relative to the exposed state (naturally doped state). This implies that more ions are accumulated closer to the substrate, which is also supported by the depth profile from XPS (Figure S11). Similar overtone dependent frequency shifts have been reported in previous mass transport studies of OMIECs using EQCM,²⁹ but has not received explicit discussion.

1

2

3

4

5

6

7

8

9

10

11

12

13

14

15

16

17

18

19

20

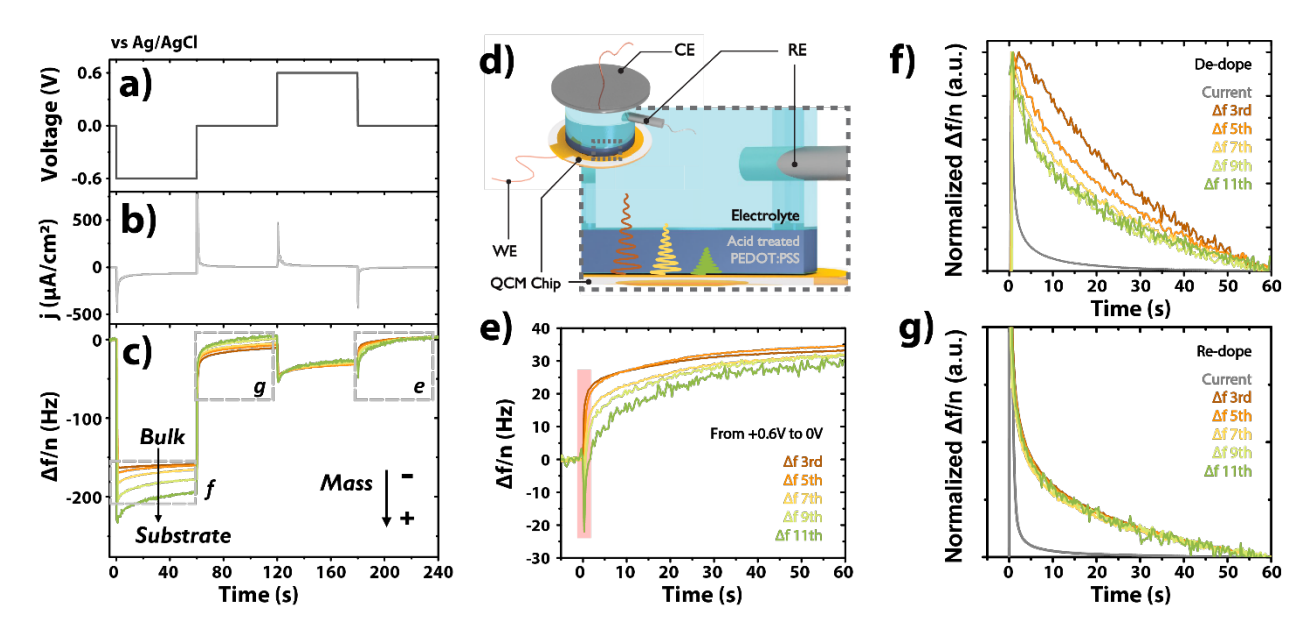


Figure 3 Potential step with time resolved EQCM for thick (~300nm) acid treated PEDOT:PSS film in electrochemical equilibrium state: a) potential profile, b) charging current density, c)

frequency shift for different overtones subtracted to the start point of the cycle. The overtones are expressed with different colors: 3rd (brown), 5th (orange), 7th (yellow), 9th (light green) and 11th (dark green); d) Schematic diagram for the setup and shear wave decay of different overtones; e)

The frequency shift of the film de-doped back to 0V from the over-doped state, from which the frequency of different overtones jumped in different directions at the start point (highlighted in red shadow). The normalized kinetics for the following slow frequency shift (mass transport) for f) de-doping process and g) re-doping process.

As with the 3^{rd} order frequency change demonstrated in **Figure 1b**, the higher-order overtones also displayed a large instantaneous (sub-second) mass change. In the de-doping and re-doping processes, this frequency shift reached more than 90% of the total shift in the first second. Although only a rough estimation of mass increase can be made from the frequency shift, we can still extract the mass change of the charged ions in the thick film by integrating the current signal spike. Taking the de-doping process as an example, if only cationic uptake contributes to ionic charge transport, the expected mass increase would be $0.06~\mu g/cm^{-2}$. However, the measured cation content by XRF is only equivalent to $0.04~\mu g/cm^{-2}$ throughout the de-doping process (calculated assuming the dry film thickness is 220 nm and a film density of $1.0~g\cdot cm^{-3}$). Therefore, anion expulsion must also contribute to the ionic charge transport in the thick film during de-doping, which is consistent with the presence of anions confirmed by XRF. At the same time, the migration of water accounts for most (>95%) of the mass change in the process.

As assessed by different overtones in EQCM, the proportion of cations and anions is not constant through the depths of the 6-layer films in this instantaneous mass transfer step. In the first dedoping process, the larger frequency shift exhibited by the higher order overtones indicates a greater mass gain in the material near the substrate. This reflects the establishment of an ion gradient during de-doping, which stems from the cation accumulation due to more cation influx caused by the instantaneous negatively polarized gold electrode. This effect is more evident when the film is de-doped back to 0 V from the over-doped state, producing the opposite direction of the initial frequency spike (**Figure 3e**). For higher order overtones (deeper in the film and closer to the substrate), an initial frequency drop (mass increase) reflected cations being drawn towards the negatively charged electrode surface, which after a few seconds was overcome by a frequency

1 increase (mass decrease) ascribed to anion expulsion. For lower order overtones (which average

the entire bulk), the anion expulsion (presumably from the shallower part of the film) dominated

across all time scales, thus exhibiting a transient mass decrease. During the opposite processes (re-

doping and over-doping, Figure 3c), the anion should be attracted to the buried positively

polarized electrode interface. In the re-doping process (Figure 3g), this transport is overshadowed

6 by the larger magnitude of cation expulsion, resulting in a net mass decrease.

2

4

5

18

19

20

21

22

23

24

25

26

27

28

29

of the film.

7 The subsequent slow process of mass transport shows a kinetic asymmetry of the de-doping and 8 re-doping processes. For the de-doping process, this slow process manifests as a slow mass decay 9 (frequency increase) after the initial mass increase spike, while for the re-doping process, the 10 process manifests as a further mass decay (frequency continues to increase) after the initial mass decrease (Figure 3c). When the film was de-doped (from 0V to -0.6V vs Ag/AgCl), the 11 12 frequencies of higher order overtones shifted more than that of the lower orders, in terms of both 13 percentage and absolute frequency difference. At the same time, the higher-order overtones 14 exhibited a faster decay rate (Figure 3f and Figure S12a-c) and a larger overall shift, indicating that ions (and water) transported away from the electrode interface faster and to a greater degree 15 16 compared to the rest of the film volume. When the film was re-doped (from -0.6 to 0V vs Ag/AgCl), different overtones showed a similar frequency decay rate (Figure 3g, perhaps even a slight 17

Putting together the above discussion, the mechanism of acid treated PEDOT:PSS during electrochemical cycles can be described as follows: in the de-doping process, polarization of the buried Au electrode induces an immediate cation flux through the film toward the buried OMIEC/electrode interface, and an opposite anion flux out of the film into the electrolyte. The rapid accumulation of cations at the OMIEC/electrode interface produces a mass gradient through the thickness of the film. As the slower process of hole extraction progresses via thermally activated hopping and charge transfer at the OMIEC/electrode interface,⁵⁹ a cation reorganization occurs to establish charge neutrality throughout the film. In the re-doping process, positive polarization of the gold electrode causes a rapid expulsion of cations out of the film and an opposite anions flux from the electrolyte into the film. The holes are then injected into the OMIEC via

inversion trend, see Figure S12d-f), representing a more uniform mass transport through the depth

1 charge transfer at the OMIEC/electrode interface, which leads to a further expulsion of cations

2 remaining in the film.

In order to better understand the proposed depth dependent ion reorganization followed the initial mass uptake/expulsion, we developed a simplified layered kinetic model (see SI Part 3, Figure S13). In the model, the film is divided into three layers in the vertical direction. In addition to the direct ion flux from/towards the external electrolyte in each layer, the cations have additional kinetic constants for diffusion between layers. This cation reorganization may be related to the binding of cations to excess PSS⁻ after the holes are neutralized and is slower than the electronic charge transport. This explains the different mass transport kinetics exhibited at different depths in the de-doping process: the ions close to the OMIEC/electrode interface yield larger apparent rate constants due to the consistent directions of the cation reorganization and anion efflux, while the ions close to the OMIEC/electrolyte interface have smaller rate constants due to the opposite directions of ion flux (Figure 2c-3). In the re-doping process, the rate constant of cations leaving the film is much larger than that of cation upward reorganization, precluding the mass reorganization process from dominating the mass transport kinetics (Figure 2d, also Figure S13c).

Mechanical/Rheological Transients

The dissipation information from EQCM-D gives more information on mechanical and rheological properties kinetics of the film.^{48, 53} Different from the frequency shift that shows a mass minimum near the naturally doped state, the dissipation decreased monotonically as the voltage increased (**Figure S14**). Considering the thickness of the film and the penetration depth of the shear wave, a double layer viscoelastic model that includes electrolyte and polymer film was used to qualitatively analyze the dissipation from the material (see **SI Part 2**).⁶⁰ In this model, the 3rd order shear wave penetrated whole polymer film with tiny decay and were completely dissipated in the bulk electrolyte (as the top layer). Based on the work by DeNolf and Sadman,^{49, 61} the elastic to viscous transient of the material can be qualitatively discussed by normalizing the ratio of the resonant frequency shift and wave dissipation (**Equation 2**, also see **SI Part 2**):

$$r_{3} = \frac{-\Delta f_{3}}{\Delta \Gamma_{3}} = \frac{-Real(\frac{\Delta f_{3}^{*}}{\Delta f_{Sauerbrey,3}})}{Imag(\frac{\Delta f_{3}^{*}}{\Delta f_{Sauerbrey,3}})}$$
(2)

- Where Δf_3^* is the complex frequency shift, and $\Delta f_{Sauerbrey,3}$ is the 3rd order frequency shift of
- Sauerbrey equation (Equation 1). The frequency dependent dissipation $\Delta\Gamma_3$ can be expressed as
- 3 Equation 3:

$$\Delta\Gamma_3 = \frac{\Delta D_3 \times f_3}{2} \tag{3}$$

- 5 The differential ratio r_3 is positively correlated to the film phase angle between 25 and 65 degrees
- 6 (**Figure S15b**), where the phase angles of common hydrated polymers locate. 62 As the r_3 increases,
- 7 the phase angle also increases, implying that the film changes from a glassy polymer to a more
- 8 Newtonian-like fluid. Thus, r_3 is selected as the rheological indicator of the acid treated
- 9 PEDOT:PSS during electrochemical cycling in the following discussion.
- In general, the increase in r_3 during the de- and over-doping of the acid treated PEDOT:PSS 10 signals an increase in the water content of the film. These steps were manifested in the $\Delta D_3 - \Delta f_3$ 11 phase plot (Figure S16a), in which the de-doping process shows a gradually r_3 change (relatively 12 constant phase angle) across voltage, while the over-doping process shows a sharp increase in the 13 r_3 across voltage, which arises from the divergent film mass and dissipation changes (**Figure S16**). 14 Focusing on the kinetics of de- and re-doping processes, similar to mass transport, these two 15 processes can be divided into a fast and a slow process, where the normalized r_3 was able to be 16 fitted in the slow process. (Figure S17) The change in r_3 in the fast and slow processes is in the 17 18 opposite direction, implying that the polymer produces an excess of rheological changes during the instantaneous voltage step and slowly returns to an equilibrium state that differs less from the 19 20 initial state over a longer period. During de-doping, the slow steps showed similar time constants across different orders, (~50s), larger than the mass change. This indicates the further mass 21 22 relaxation is not closely related to the cation distribution. During re-doping, the relaxation of film phase angle is also slower than the mass transport. The relaxation of the material rheology is 23 24 always going on after the other processes have reached equilibrium, which may be accompanied by mesoscale structure changes within the material. 25

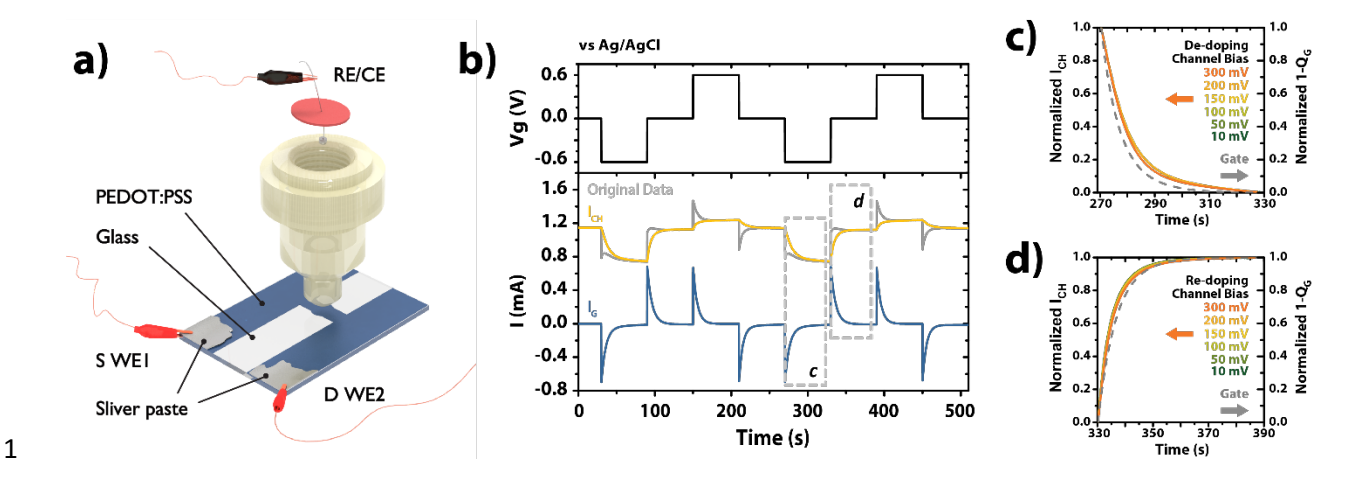


Figure 4 Pseudo OECT measurement and the results: a) cone cell used for OECT measurements, and the patterned acid treated PEDOT:PSS chip; b) electrochemical cycling of the OECT at V_{S-D} =10mV. The channel current (yellow) and gate current (blue) were deconvoluted from source and drain current (grey, see the discussion in **SI Part 4**). The normalized channel current together with the gate current for c) de-doping and d) re-doping process, showing the channel current under different channel voltages, V_{DS} (solid-colored lines) and the gate current (dash grey lines).

Charge Transport Transients

For OECTs, mass and charge transport are not the only parameters to be concerned with; the formation of effective macroscopic charge transport pathways is also very important. Using a cone cell consistent with the previously reported operando GIWAXS (**Figure 4a**),²⁶ the same stepped potential patterns as EQCM-D measurements were applied to the patterned, acid treated PEDOT:PSS with the channel biased in the linear regime (**Figure 4a**). The charging current is deconvoluted from the S-D current of the device (**Figure 4b** and **SI Part 4**).⁶³ The transient changes and equilibrium states of channel conductivity with different S-D biases were found to be approximately the same (**Figure S18**).

To further analyze the change in hole mobility of the material during individual electrochemical steps, we calculate the differential mobility from the incremental change in conductivity and charge density (see **SI Part 4**). From the differential mobility, we can compare the effective mobility of the added/extracted carriers during electrochemical cycling. When applied potential decreases the charge density (de-doping and returning of 0V from over-doped state), conductivity

decreases faster than charge density (Figure 4c, Figure S19b), implying that high mobility charge 1 2 carriers are extracted first. Conversely, with potential steps increasing the charge density (re-3 doping and over-doping), conductivity increases slightly faster than charge density (Figure 4d, Figure S19a), indicating that the initial injected charge carriers have a higher effective mobility 4 than successive injected carriers. This is rationalized as due to the increased energetic and 5 structural disorder that accompanies increased dopant and charge carrier densities, which 6 diminishes hole mobility.⁶⁴ Additionally, the differential mobility in de-doping and re-doping 7 processes is larger than that in over-doping process as hole density increased after over-doping 8 (Figure S20), implying that the DOS of the doped acid treated PEDOT:PSS is over half-full.⁶⁵ 9

The electric field profile change caused by ionic lateral transport is negligible for the kinetics of the channel current decay. When a large D-S voltage saturates the channel, the non-equilibrium lateral ion current may affect the distribution of holes and thus change the kinetics of the channel current. 66 However, the very small D-S voltage (10mV) in our measurements still show the kinetic asymmetry between de-doping and re-doping process. The amount of charge extracted from drain and source electrode is nearly equal (~50%) when the D-S voltage is small (10mV and 50mV), implying the channel material is in the linear region and far from saturation (Table S3). This kinetic asymmetry persisted as the D-S voltage increased, where the time constant of the de-doping process slightly decreased and the time constant of the re-doping process slightly increased (Figure S19c). The asymmetry of the charge transport kinetics during de-doping and re-doping processes observed in OECT is consistent with the results in EQCM (Figure 2b). This asymmetry may originate from a difference in driving force applied. The threshold voltage of PEDOT:PSS is closer to the voltage in de-doped state than that in re-doped state,²² which likely results in a slower charge transport in de-doping than that in re-doping. The above experimental results all indicate that the change in hole mobility, rather than the change in electric field due to ion migration/ reorganization, is the rate-determining factor in channel current kinetics.

The sequence of mass, charge, and structure kinetics

10

11

12

13

14

15

16

17

18

19

20

21

22

23

24

25

26

27

28

29

30

As OMIEC charging and discharging occur via an RC process, the kinetic data across experiments can be compared by normalizing with the individual experiment RC time constants (τ_{RC}) in order to compare different dataset at similar degrees of charging. In this study, transient behavior of mass (manifest as normalized frequency shift), rheological properties (manifest as r_3), channel

conductivity, and effective mobility were aligned to the previously reported transient data of molecular packing (manifest in the lamellar d-spacing), and UV-visible optical spectra (polaron/neutral population) (**Table S4**). In all cases, an exponential or double exponential fit was used to extract the time constant τ , and all these fits yielded good agreement with observed functionality (**Figure 5**). The mass transport process is the fastest compared to other processes, which is not necessarily expected in OMIECs. In general, this is consistent with studies of P3HT from Flagg et al which showed that mass transport is faster than hole injection.⁴³ However, the overall time constants here are much faster than that of P3HT due to the faster ion transport in the more hydrophilic acid treated PEDOT:PSS.



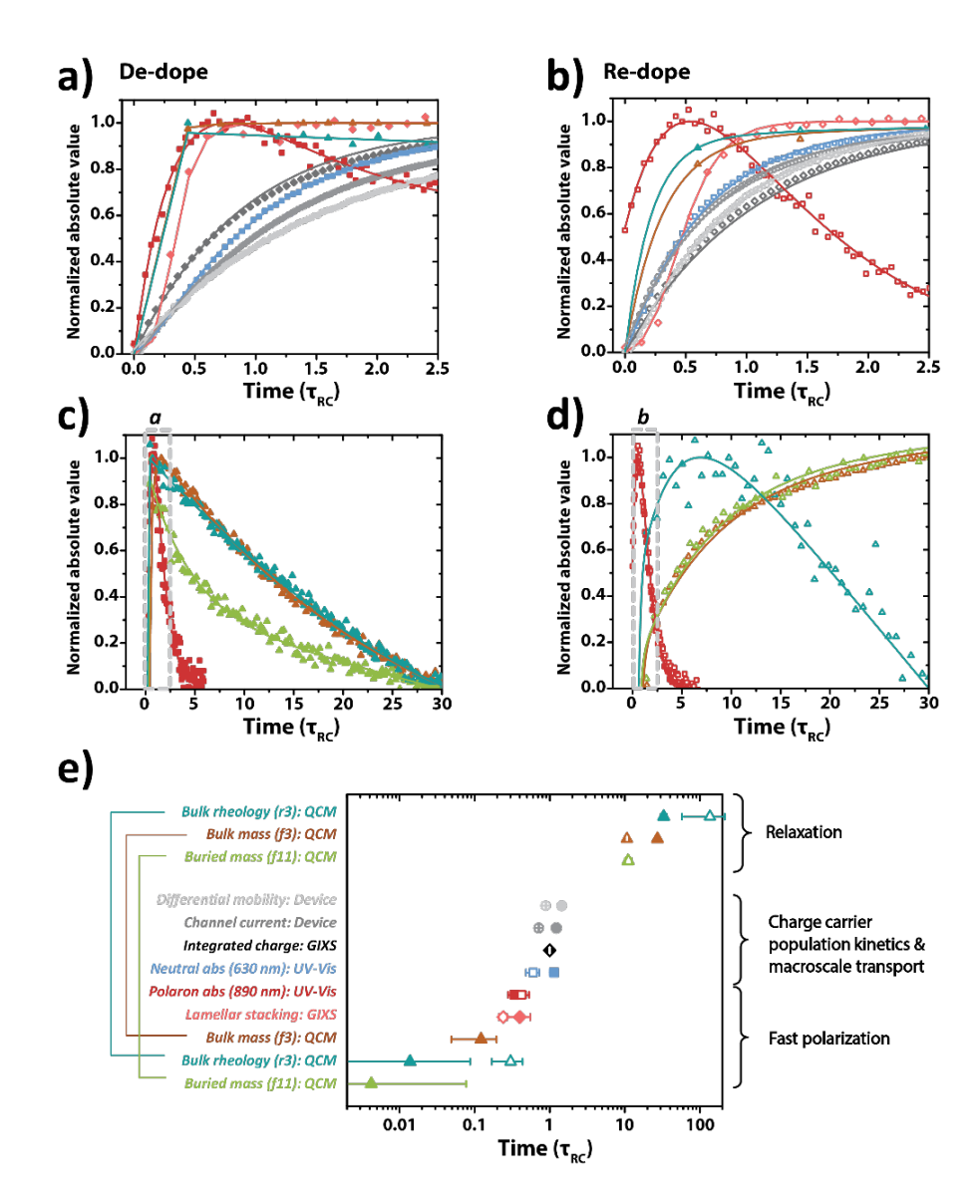


Figure 5 RC normalized curves between $0\tau_{RC}$ to $2.5\tau_{RC}$ for a) de-doping process and b) re-doping process to show the order of fast polarization, charge carrier population kinetics and macroscale transport. RC normalized curves between $0\tau_{RC}$ to $30\tau_{RC}$ for c) de-doping process and d) re-doping process to show the order of slow macroscale mass and rheological relaxation. In a-d, data are shown as symbols, solid lines represent the exponential/double exponential fits. The color scheme corresponds to the techniques/processes listed in the legend in (e). e) RC normalized time constants for de-doping (filled symbols) and re-doping (open symbols) processes. The error bars shown are the larger of either the 95% confidence interval of the fit parameters, or single time step for each measurement. In this figure, the triangles, circles, diamonds, and squares are experimental data points. The triangles are from EQCM measurement; the circles are from the pseudo OECT measurement; the diamonds are from in situ GIWAXS measurement; and the squares are from optical measurements. Colors correspond to: integrated charge (black), channel current (grey), differential mobility (light grey), lamellar spacing (light red), polaron absorption (dark red), neutral absorption (light blue), bulk mass change (brown), rheological property change (cyan) and deep layer mass change (light green).

In the de-doping process of the material (**Figure 5a**), the film mass, rheological properties and initial polaron/bipolarons concentration changes are closely overlayed and in an extremely short time scale ($<0.2\tau_{RC}$), indicating that these three factors are strongly sensitive to the polarization of the buried electrode, and their response precedes any significant changes in hole density. The rapid response of these three is immediately followed by the lamellar expansion within the crystalline domains as assessed by in situ GIWAXS ($<0.5\tau_{RC}$). The slower charge extraction continued throughout, accompanied by the growth of neutral species absorption and successive bleach of the polaron absorption. The decrease in film conductivity and the increase in effective hole mobility are further slower than the charge transfer (**Figure S20a-b**). In analyzing the temporal error, the main source of uncertainty was identified to be the relative onset of the mass and rheological transients with respect to the polaron absorption and lamellar contraction transients (see **SI Part 5** for detailed discussion). That they (mass and rheological property transients) occur rapidly and precede all others (charge, neutral absorption, channel current, and differential mobility transients) is determined with certainty.

- In the re-doping process (Figure 5b), the large mass decrease and concomitant rheological property changes again are the most rapid processes, which is overlayed with the conversion of neutral species to polarons. The polarons then further convert into bipolarons, which is associated with the reduction of the lamellar spacing. Lagging behind this is the bleach rate of neutral species, and the increase in channel current, differential mobility, and film charging, in that order. The difference between the neutral bleach and channel current transients is minimal such that their relative order cannot be determined with certainty, however, both processes are significantly faster than the differential mobility and charging current transients.
 - While the mass and rheological responses are large and rapid, they both display a slow relaxation process spanning tens of τ_{RC} . In the de-doping process, the mass transfer near the buried OMIEC/electrode interface takes the lead in equilibrium (**Figure 5c**). The equilibrium time constants for rheology (r_3) and mass transport in the bulk material are similar, and both are remarkably longer than the mass transport material near the OMIEC/electrode interface. This is because the dissipation change (as the denominator of r_3) in this process is small, allowing the rheological kinetics to be consistent with the mass transport kinetics in the bulk film (as the numerator of r_3). In the re-doping process, the kinetic rates of mass transfer are similar at different depths, while the overall film rheological properties remain far from equilibrium after the mass transfer reaches the equilibrium state (**Figure 5d**), indicating that there are long term mesoscale relaxations occurring on the order of minutes.
 - Summarized in **Figure 5e**, we plot the extracted time constants of the above-mentioned transients on a $\log \tau_{RC}$ time scale and label the errors of each time constant based on the corresponding error discussion. The de-doping and re-doping processes can be clustered into three sub processes: the fast polarization of the electrode and OMIEC materials, charge carrier population kinetics and macroscale transport, and the slow relaxation. In the de-doping process, the boundaries of all three processes are clear. In the re-doping process, there is time overlap between two fast sub processes, but the time scale of the slow relaxation is still dramatically different.

Conclusions

This work investigates compositional, mass, rheological, and charging transients in a prototypical OMIEC material, acid treated PEDOT:PSS during electrochemical cycling, building on previous operando X-ray scattering and EQCM works on OMIECs. With EQCM-D, we investigate the mass transport in relation to charge, conductivity, carrier concentration and microstructure. In OMIECs, the transients of the mass transport and rheological properties and the conversion of polaron/bipolarons are the fastest process. By comparing different overtones from EQCM-D data, we reveal the depth dependence of the fast mass transients and point out the ion reorganization process later. Finally, we establish an order of operations in response to changes in electrochemical potential: the mass/rheological properties, polaron concentration, and microstructure respond first, followed by the charge accumulation, neutral absorption, and macroscopic conductivity changes; with the relative order of the latter depending on whether the film is undergoing doping or dedoping. These results open the door to further inquiry into the kinetics of OMIEC structure and rheology. For example, this work invites further dedicated rheological experiments to produce quantitative rheological models, and highlight the need for future studies to connect rheological properties with in situ/operando meso-scale structural characterization (such as neutron scattering, small angle X-ray scattering and X-ray photon correlation spectroscopy). Further, the mapping of properties over relatively long timescales should be combined with future ultrafast studies to investigate the discrete processes underlying the kinetics discussed here. Finally, as OMIECs are a diverse class of materials, similar studies on other OMIEC material classes (e.g., conjugated polyelectrolytes, conjugated polymer electrolytes, small molecules, etc.) will inform the generality the observed kinetics. The results reported here not only provide insight into the operation mechanism of acid treated PEDOT:PSS, but also reveal the factors affecting the response time of OMIEC devices, guiding the future design of OMIEC materials.

24

25

1

2

3

4

5

6

7

8

9

10

11

12

13

14

15

16

17 18

19

20

21

22

23

Author Information

26 Corresponding Author

- 27 Jonathan Rivnay Dept. of Biomedical Engineering, Northwestern University, Evanston, Illinois
- 28 60208, United States; Simpson Querrey Institute, Northwestern University, Chicago, Illinois
- 29 60611, United States;

- 1 ORCID: https://orcid.org/0000-0002-0602-6485; Email: jrivnay@northwestern.edu
- 2 Authors
- 3 Ruiheng Wu Dept. of Chemistry, Northwestern University, Evanston, Illinois 60208, United
- 4 States;
- 5 ORCID: https://orcid.org/0000-0003-2666-6110
- 6 Bryan D. Paulsen Dept. of Biomedical Engineering, Northwestern University, Evanston, Illinois
- 7 60208, United States;
- 8 ORCID: https://orcid.org/0000-0002-0923-8475
- 9 Qing Ma DND-CAT, Synchrotron Research Center, Northwestern University, Evanston, Illinois,
- 10 60208, United States.
- 11 Notes

17

18

12 The authors declare no competing financial interest.

14 Supporting Information

- 15 Additional information for EQCM model for thick OMIEC film, cation reorganization kinetic
- model, differential mobility calculation and certainty analysis. (PDF)

Acknowledgments

- 19 R.W., B.D.P., and J.R. acknowledge support from the National Science Foundation grant no. NSF
- 20 DMR-1751308. This work utilized the Keck-II facility of Northwestern University's NUANCE
- 21 Center, supported by the Soft and Hybrid Nanotechnology Experimental (SHyNE) Resource (NSF
- 22 ECCS-1542205), the Materials Research Science and Engineering Center (NSF DMR-1720139),
- 23 the State of Illinois, and Northwestern University. Additionally, the Keck-II facility is partially
- supported by the International Institute for Nanotechnology (IIN); the Keck Foundation; and the
- 25 State of Illinois, through the IIN. The X-ray fluorescence characterization is performed at the 5-

- 1 BM-D beamline of the DuPont-Northwestern-Dow Collaborative Access Team (DND-CAT)
- 2 located at Sector 5 of the Advanced Photon Source (APS). DND-CAT is supported by
- 3 Northwestern University, The Dow Chemical Company, and DuPont de Nemours, Inc. This
- 4 research used resources at the APS, a U.S. Department of Energy (DOE) Office of Science User
- 5 Facility operated by Argonne National Laboratory under Contract No. DE-AC02-06CH11357.

7

References

- 8 1. Paulsen, B. D.; Tybrandt, K.; Stavrinidou, E.; Rivnay, J., Organic Mixed Ionic–Electronic
- 9 Conductors. *Nature Materials* **2020,** *19*, 13-26.
- 2. Quek, G.; Roehrich, B.; Su, Y.; Sepunaru, L.; Bazan, G. C., Conjugated Polyelectrolytes:
- 11 Underexplored Materials for Pseudocapacitive Energy Storage. Advanced Materials 2022, 34
- 12 2104206.
- 3. Samuel, J. J.; Karrothu, V. K.; Canjeevaram Balasubramanyam, R. K.; Mohapatra, A. A.;
- Gangadharappa, C.; Kankanallu, V. R.; Patil, S.; Aetukuri, N. P. B., Ionic Charge Storage in
- 15 Diketopyrrolopyrrole-Based Redox-Active Conjugated Polymers. *The Journal of Physical*
- 16 *Chemistry C* **2021,** *125*, 4449-4457.
- 4. van Dijken, A.; Perro, A.; Meulenkamp, E. A.; Brunner, K., The Influence of a PEDOT: PSS
- Layer on the Efficiency of a Polymer Light-Emitting Diode. *Org Electron* **2003**, *4*, 131-141.
- 5. Edman, L.; Summers, M. A.; Buratto, S. K.; Heeger, A. J., Polymer Light-Emitting
- 20 Electrochemical Cells: Doping, Luminescence, and Mobility. *Phys Rev B* **2004**, *70*, 115212.
- 21 6. Matyba, P.; Maturova, K.; Kemerink, M.; Robinson, N. D.; Edman, L., The Dynamic
- Organic P-N Junction. *Nature Materials* **2009**, *8*, 672-676.
- 7. Okuzaki, H.; Takagi, S.; Hishiki, F.; Tanigawa, R., Ionic Liquid/Polyurethane/PEDOT:PSS
- 24 Composites for Electro-Active Polymer Actuators. Sensor Actuat B-Chem 2014, 194, 59-63.
- 8. Rivnay, J.; Inal, S.; Salleo, A.; Owens, R. M.; Berggren, M.; Malliaras, G. G., Organic
- Electrochemical Transistors. *Nat Rev Mater* **2018**, *3*, 17086.
- 27 9. Chun, H. G.; Chung, T. D., Iontronics. *Annu Rev Anal Chem* **2015**, *8*, 441-462.
- 28 10. Williamson, A.; Ferro, M.; Leleux, P.; Ismailova, E.; Kaszas, A.; Doublet, T.; Quilichini,
- 29 P.; Rivnay, J.; Rózsa, B.; Katona, G., et al., Localized Neuron Stimulation with Organic

- 1 Electrochemical Transistors on Delaminating Depth Probes. *Advanced Materials* **2015**, *27*, 4405-
- 2 4410.
- 3 11. Proctor, C. M.; Uguz, I.; Slezia, A.; Curto, V.; Inal, S.; Williamson, A.; Malliaras, G. G.,
- 4 An Electrocorticography Device with an Integrated Microfluidic Ion Pump for Simultaneous
- 5 Neural Recording and Electrophoretic Drug Delivery in Vivo. *Advanced Biosystems* **2019**, *3*,
- 6 1800270.
- 7 12. Strakosas, X.; Bongo, M.; Owens, R. M., The Organic Electrochemical Transistor for
- 8 Biological Applications. *Journal of Applied Polymer Science* **2015**, *132*, 41735.
- 9 13. Kim, N.; Kee, S.; Lee, S. H.; Lee, B. H.; Kahng, Y. H.; Jo, Y. R.; Kim, B. J.; Lee, K.,
- 10 Highly Conductive PEDOT: PSS Nanofibrils Induced by Solution-Processed Crystallization.
- 11 *Advanced Materials* **2014,** *26*, 2268-2272.
- 14. Ouyang, J.; Xu, Q. F.; Chu, C. W.; Yang, Y.; Li, G.; Shinar, J., On the Mechanism of
- 13 Conductivity Enhancement in Poly (3,4-Ethylenedioxythiophene): Poly(Styrene Sulfonate) Film
- through Solvent Treatment. *Polymer* **2004,** *45*, 8443-8450.
- 15. Hakansson, A.; Han, S. B.; Wang, S. H.; Lu, J.; Braun, S.; Fahlman, M.; Berggren, M.;
- 16 Crispin, X.; Fabiano, S., Effect of (3-Glycidyloxypropyl)Trimethoxysilane (Gops) on the
- 17 Electrical Properties of PEDOT:PSS Films. *J Polym Sci Pol Phys* **2017**, *55*, 814-820.
- 18 16. Lingstedt, L. V.; Ghittorelli, M.; Lu, H.; Koutsouras, D. A.; Marszalek, T.; Torricelli, F.;
- 19 Craciun, N. I.; Gkoupidenis, P.; Blom, P. W. M., Effect of Dmso Solvent Treatments on the
- 20 Performance of PEDOT:PSS Based Organic Electrochemical Transistors. *Adv Electron Mater*
- **2019,** *5*, 1800804.
- 17. Shi, H.; Liu, C. C.; Jiang, Q. L.; Xu, J. K., Effective Approaches to Improve the Electrical
- 23 Conductivity of PEDOT:PSS: A Review. *Adv Electron Mater* **2015,** *1*, 1500017.
- 24 18. Xu, S. D.; Hong, M.; Shi, X. L.; Wang, Y.; Ge, L.; Bai, Y.; Wang, L. Z.; Dargusch, M.;
- 25 Zou, J.; Chen, Z. G., High-Performance PEDOT: PSS Flexible Thermoelectric Materials and
- Their Devices by Triple Post-Treatments. *Chem Mater* **2019**, *31*, 5238-5244.
- 27 19. Hosseini, E.; Kollath, V. O.; Karan, K., The Key Mechanism of Conductivity in
- 28 PEDOT:PSS Thin Films Exposed by Anomalous Conduction Behaviour Upon Solvent-Doping
- and Sulfuric Acid Post-Treatment. J Mater Chem C 2020, 8, 3982-3990.
- 30 20. Inal, S.; Malliaras, G. G.; Rivnay, J., Benchmarking Organic Mixed Conductors for
- 31 Transistors. *Nat Commun* **2017,** *8*, 1767.

- 1 21. Zhang, M.; Zhou, Q. Q.; Chen, J.; Yu, X. W.; Huang, L.; Li, Y. R.; Li, C.; Shi, G. Q., An
- 2 Ultrahigh-Rate Electrochemical Capacitor Based on Solution-Processed Highly Conductive
- 3 PEDOT:PSS Films for Ac Line-Filtering. *Energ Environ Sci* **2016**, *9*, 2005-2010.
- 4 22. Kim, Y.; Noh, H.; Paulsen, B. D.; Kim, J.; Jo, I. Y.; Ahn, H.; Rivnay, J.; Yoon, M. H.,
- 5 Strain-Engineering Induced Anisotropic Crystallite Orientation and Maximized Carrier Mobility
- 6 for High-Performance Microfiber-Based Organic Bioelectronic Devices. Advanced Materials
- **2021,** *33*, 2007550.
- 8 23. Lee, J. H.; Jeong, Y. R.; Lee, G.; Jin, S. W.; Lee, Y. H.; Hong, S. Y.; Park, H.; Kim, J.
- 9 W.; Lee, S. S.; Ha, J. S., Highly Conductive, Stretchable, and Transparent PEDOT:PSS
- 10 Electrodes Fabricated with Triblock Copolymer Additives and Acid Treatment. Acs Appl Mater
- 11 *Inter* **2018,** *10*, 28027-28035.
- 12 24. Jeong, W.; Park, Y.; Gwon, G.; Song, J.; Yoo, S.; Bae, J.; Ko, Y. H.; Choi, J. H.; Lee, S.,
- 13 All-Organic, Solution-Processed, Extremely Conformal, Mechanically Biocompatible, and
- Breathable Epidermal Electrodes. *Acs Appl Mater Inter* **2021**, *13*, 5660-5667.
- 25. Paulsen, B. D.; Fabiano, S.; Rivnay, J., Mixed Ionic-Electronic Transport in Polymers. Annu
- 16 Rev Mater Res **2021**, *51*, 73-99.
- 26. Paulsen, B. D.; Wu, R. H.; Takacs, C. J.; Steinruck, H. G.; Strzalka, J.; Zhang, Q. T.;
- 18 Toney, M. F.; Rivnay, J., Time-Resolved Structural Kinetics of an Organic Mixed Ionic-
- 19 Electronic Conductor. *Advanced Materials* **2020,** *32*, 2003404.
- 20 27. Rivnay, J.; Inal, S.; Collins, B. A.; Sessolo, M.; Stavrinidou, E.; Strakosas, X.; Tassone,
- 21 C.; Delongchamp, D. M.; Malliaras, G. G., Structural Control of Mixed Ionic and Electronic
- Transport in Conducting Polymers. *Nat Commun* **2016,** 7, 11287.
- 28. Giridharagopal, R.; Flagg, L. Q.; Harrison, J. S.; Ziffer, M. E.; Onorato, J.; Luscombe, C.
- 24 K.; Ginger, D. S., Electrochemical Strain Microscopy Probes Morphology-Induced Variations in
- 25 Ion Uptake and Performance in Organic Electrochemical Transistors. *Nature Materials* **2017**, *16*,
- 26 737.
- 29. Savva, A.; Wustoni, S.; Inal, S., Ionic-to-Electronic Coupling Efficiency in PEDOT:PSS
- Films Operated in Aqueous Electrolytes. *J Mater Chem C* **2018**, *6*, 12023-12030.
- 29 30. Kim, S. M.; Kim, C. H.; Kim, Y.; Kim, N.; Lee, W. J.; Lee, E. H.; Kim, D.; Park, S.;
- 30 Lee, K.; Rivnay, J., et al., Influence of PEDOT:PSS Crystallinity and Composition on
- Electrochemical Transistor Performance and Long-Term Stability. *Nat Commun* **2018**, *9*, 3858.

- 1 31. Wu, R.; Matta, M.; Paulsen, B. D.; Rivnay, J., Operando Characterization of Organic Mixed
- 2 Ionic/Electronic Conducting Materials. *Chemical Reviews* **2022**, *122*, 4493-4551.
- 3 32. Rebetez, G.; Bardagot, O.; Affolter, J.; Rehault, J.; Banerji, N., What Drives the Kinetics
- 4 and Doping Level in the Electrochemical Reactions of PEDOT:PSS? Adv Funct Mater 2021, 32,
- 5 2105821.
- 6 33. Bernards, D. A.; Malliaras, G. G., Steady-State and Transient Behavior of Organic
- 7 Electrochemical Transistors. *Adv Funct Mater* **2007**, *17*, 3538-3544.
- 8 34. Shirinskaya, A.; Horowitz, G.; Rivnay, J.; Malliaras, G. G.; Bonnassieux, Y., Numerical
- 9 Modeling of an Organic Electrochemical Transistor. *Biosensors-Basel* **2018**, *8*, 103.
- 35. Friedlein, J. T.; McLeod, R. R.; Rivnay, J., Device Physics of Organic Electrochemical
- 11 Transistors. *Org Electron* **2018**, *63*, 398-414.
- 36. Stavrinidou, E.; Leleux, P.; Rajaona, H.; Khodagholy, D.; Rivnay, J.; Lindau, M.; Sanaur,
- 13 S.; Malliaras, G. G., Direct Measurement of Ion Mobility in a Conducting Polymer. *Advanced*
- 14 *Materials* **2013,** *25*, 4488-4493.
- 37. Friedlein, J. T.; Shaheen, S. E.; Malliaras, G. G.; McLeod, R. R., Optical Measurements
- 16 Revealing Nonuniform Hole Mobility in Organic Electrochemical Transistors. *Adv Electron*
- 17 *Mater* **2015,** *I*, 1500189.
- 18 38. Savva, A.; Cendra, C.; Giugni, A.; Torre, B.; Surgailis, J.; Ohayon, D.; Giovannitti, A.;
- 19 McCulloch, I.; Di Fabrizio, E.; Salleo, A., et al., Influence of Water on the Performance of
- 20 Organic Electrochemical Transistors. *Chem Mater* **2019**, *31*, 927-937.
- 21 39. Savva, A.; Hallani, R.; Cendra, C.; Surgailis, J.; Hidalgo, T. C.; Wustoni, S.;
- Sheelamanthula, R.; Chen, X. X.; Kirkus, M.; Giovannitti, A., et al., Balancing Ionic and
- 23 Electronic Conduction for High-Performance Organic Electrochemical Transistors. Adv Funct
- 24 *Mater* **2020**, *30*, 1907657.
- 25 40. Cendra, C.; Giovannitti, A.; Savva, A.; Venkatraman, V.; McCulloch, I.; Salleo, A.; Inal,
- 26 S.; Rivnay, J., Role of the Anion on the Transport and Structure of Organic Mixed Conductors.
- 27 Adv Funct Mater **2019**, 29, 1807034.
- 41. Moser, M.; Hidalgo, T. C.; Surgailis, J.; Gladisch, J.; Ghosh, S.; Sheelamanthula, R.;
- 29 Thiburce, Q.; Giovannitti, A.; Salleo, A.; Gasparini, N., et al., Side Chain Redistribution as a
- 30 Strategy to Boost Organic Electrochemical Transistor Performance and Stability. *Advanced*
- 31 *Materials* **2020,** *32*, 2002748.

- 42. Surgailis, J.; Savva, A.; Druet, V.; Paulsen, B. D.; Wu, R. H.; Hamidi-Sakr, A.; Ohayon,
- 2 D.; Nikiforidis, G.; Chen, X. X.; McCulloch, I., et al., Mixed Conduction in an N-Type
- 3 Organic Semiconductor in the Absence of Hydrophilic Side-Chains. *Adv Funct Mater* **2021,** *31*,
- 4 2010165.
- 5 43. Flagg, L. Q.; Giridharagopal, R.; Guo, J. J.; Ginger, D. S., Anion-Dependent Doping and
- 6 Charge Transport in Organic Electrochemical Transistors. *Chem Mater* **2018**, *30*, 5380-5389.
- 7 44. Thakur, R. M.; Easley, A. D.; Wang, S. Y.; Zhang, Y. R.; Ober, C. K.; Lutkenhaus, J. L.,
- 8 Real Time Quantification of Mixed Ion and Electron Transfer Associated with the Doping of
- 9 Poly(3-Hexylthiophene). *J Mater Chem C* **2022**, *10*, 7251-7262.
- 45. Creager, S., Solvents and Supporting Electrolytes. *Handbook of Electrochemistry* **2007**, 57-
- 11 72.
- 46. Paulsen, B. D.; Wu, R.; Takacs, C. J.; Steinrück, H. G.; Strzalka, J.; Zhang, Q.; Toney,
- 13 M. F.; Rivnay, J., Time-Resolved Structural Kinetics of an Organic Mixed Ionic–Electronic
- 14 Conductor. *Advanced Materials* **2020,** *32*, 2003404.
- 47. Cao-Paz, A. M.; Rodriguez-Pardo, L.; Farina, J.; Marcos-Acevedo, J., Resolution in QCM
- Sensors for the Viscosity and Density of Liquids: Application to Lead Acid Batteries. Sensors-
- 17 *Basel* **2012,** *12*, 10604-10620.
- 48. Easley, A. D.; Ma, T.; Eneh, C. I.; Yun, J.; Thakur, R. M.; Lutkenhaus, J. L., A Practical
- 19 Guide to Quartz Crystal Microbalance with Dissipation Monitoring of Thin Polymer Films. J
- 20 *Polym Sci* **2022,** *60*, 1090–110.
- 49. DeNolf, G. C.; Sturdy, L. F.; Shull, K. R., High-Frequency Rheological Characterization of
- Homogeneous Polymer Films with the Quartz Crystal Microbalance. *Langmuir* **2014**, *30*, 9731-
- 23 9740.
- 50. Voinova, M. V.; Rodahl, M.; Jonson, M.; Kasemo, B., Viscoelastic Acoustic Response of
- 25 Layered Polymer Films at Fluid-Solid Interfaces: Continuum Mechanics Approach. *Phys Scripta*
- 26 **1999,** *59*, 391-396.
- 51. Sadman, K.; Wiener, C. G.; Weiss, R. A.; White, C. C.; Shull, K. R.; Vogt, B. D.,
- 28 Quantitative Rheometry of Thin Soft Materials Using the Quartz Crystal Microbalance with
- 29 Dissipation. *Anal Chem* **2018,** *90*, 4079-4088.

- 52. Ma, T.; Easley, A. D.; Wang, S. Y.; Flouda, P.; Lutkenhaus, J. L., Mixed Electron-Ion-
- 2 Water Transfer in Macromolecular Radicals for Metal-Free Aqueous Batteries. Cell Rep Phys
- 3 *Sci* **2021,** *2*, 100414.
- 4 53. Wang, S. Y.; Li, F.; Easley, A. D.; Lutkenhaus, J. L., Real-Time Insight into the Doping
- 5 Mechanism of Redox-Active Organic Radical Polymers. *Nature Materials* **2019**, *18*, 69.
- 6 54. Zhang, L. S.; Andrew, T. L., Deposition Dependent Ion Transport in Doped Conjugated
- 7 Polymer Films: Insights for Creating High-Performance Electrochemical Devices. *Adv Mater*
- 8 *Interfaces* **2017**, *4*, 1700873.
- 9 55. Matta, M.; Wu, R.; Paulsen, B. D.; Petty, A. J.; Sheelamanthula, R.; McCulloch, I.;
- 10 Schatz, G. C.; Rivnay, J., Ion Coordination and Chelation in a Glycolated Polymer
- 11 Semiconductor: Molecular Dynamics and X-Ray Fluorescence Study. *Chem Mater* **2020,** *32*,
- *7301-7308*.
- 56. Flagg, L. Q.; Bischak, C. G.; Quezada, R. J.; Onorato, J. W.; Luscombe, C. K.; Ginger, D.
- 14 S., P-Type Electrochemical Doping Can Occur by Cation Expulsion in a High-Performing
- Polymer for Organic Electrochemical Transistors. *Acs Mater Lett* **2020,** *2*, 254-260.
- 57. Spyropoulos, G. D.; Gelinas, J. N.; Khodagholy, D., Internal Ion-Gated Organic
- 17 Electrochemical Transistor: A Building Block for Integrated Bioelectronics. *Sci Adv* **2019**, *5*,
- 18 7378.
- 19 58. Galuska, L. A.; Muckley, E. S.; Cao, Z. Q.; Ehlenberg, D. F.; Qian, Z. Y.; Zhang, S.;
- 20 Rondeau-Gagne, S.; Phan, M. D.; Ankner, J. F.; Ivanov, I. N., et al., SMART Transfer Method
- 21 to Directly Compare the Mechanical Response of Water-Supported and Free-Standing Ultrathin
- 22 Polymeric Films. *Nat Commun* **2021**, *12*, 2347.
- 59. Coropceanu, V.; Cornil, J.; da Silva, D. A.; Olivier, Y.; Silbey, R.; Bredas, J. L., Charge
- 24 Transport in Organic Semiconductors (Vol 107, Pg 926, 2007). Chemical Reviews 2007, 107,
- 25 2165-2165.
- 26 60. Martin, E. J.; Mathew, M. T.; Shull, K. R., Viscoelastic Properties of Electrochemically
- 27 Deposited Protein/Metal Complexes. *Langmuir* **2015**, *31*, 4008-4017.
- 28 61. Sadman, K.; Wang, Q.; Chen, S. H.; Delgado, D. E.; Shull, K. R., Ph-Controlled
- 29 Electrochemical Deposition of Polyelectrolyte Complex Films. *Langmuir* **2017**, *33*, 1834-1844.
- 30 62. Sadman, K.; Wang, Q.; Chen, Y.; Keshavarz, B.; Jiang, Z.; Shull, K. R., Influence of
- 31 Hydrophobicity on Polyelectrolyte Complexation. *Macromolecules* **2017**, *50*, 9417-9426.

- 1 63. Friedlein, J. T.; Donahue, M. J.; Shaheen, S. E.; Malliaras, G. G.; McLeod, R. R.,
- 2 Microsecond Response in Organic Electrochemical Transistors: Exceeding the Ionic Speed
- 3 Limit. *Advanced Materials* **2016**, *28*, 8398-8404.
- 4 64. Paulsen, B. D.; Frisbie, C. D., Dependence of Conductivity on Charge Density and
- 5 Electrochemical Potential in Polymer Semiconductors Gated with Ionic Liquids. J Phys Chem C
- 6 **2012,** *116*, 3132-3141.
- 7 65. Friedlein, J. T.; Rivnay, J.; Dunlap, D. H.; McCulloch, I.; Shaheen, S. E.; McLeod, R. R.;
- 8 Malliaras, G. G., Influence of Disorder on Transfer Characteristics of Organic Electrochemical
- 9 Transistors. *Appl Phys Lett* **2017**, *111*, 023301.
- 10 66. Kaphle, V.; Paudel, P. R.; Dahal, D.; Radha Krishnan, R. K.; Lüssem, B., Finding the
- Equilibrium of Organic Electrochemical Transistors. *Nat Commun* **2020,** *11*, 2515.

13 For Table of Contents Only

